

Correlating Antiagglomerant Performance with Gas Hydrate Cohesion

Anh Phan,¹ Michail Stamatakis,¹ Carolyn A. Koh² and Alberto Striolo^{1,*}

¹Department of Chemical Engineering, University College London, London WC1E 7JE, UK

²Center for Hydrate Research, Chemical & Biological Engineering Department, Colorado School of Mines, Golden, Colorado 80401, United States

*Corresponding Author

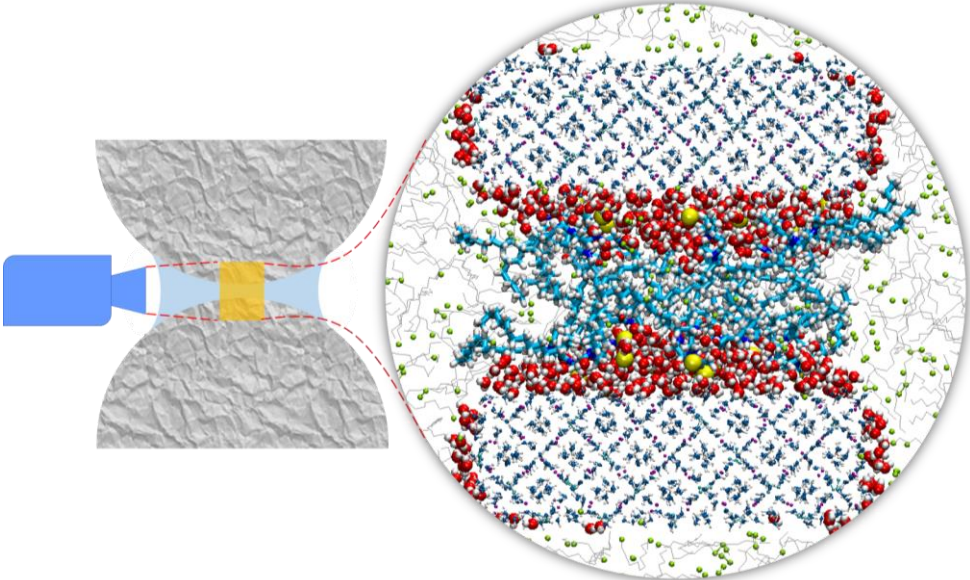
a.striolo@ucl.ac.uk

Keywords: Molecular dynamics, configurational entropy, cohesive force, gas hydrate agglomeration, enthalpy of solvation, solvation free energy

Abstract

Although inhibiting hydrate formation in hydrocarbon-water systems is paramount in preventing pipe blockage in hydrocarbon transport systems, the molecular mechanisms responsible for antiagglomerant performance are not completely understood. To better understand why macroscopic performance is affected by apparently small changes in the antiagglomerant molecular structure, we perform molecular dynamics simulations. We quantify the cohesion energy between two gas hydrate nano-particles dispersed in liquid hydrocarbons in the presence of different antiagglomerants, and we achieve excellent agreement against experimental data obtained at high pressure using the micromechanical force apparatus. This suggests that the proposed simulation approach could provide a screening method for predicting, *in silico*, the performance of new molecules designed to manage hydrates in flow assurance. Our results suggest that entropy and free energy of solvation of AAs, combined in some cases with the molecular orientation at hydrate-oil interfaces, are descriptors that could be used to predict performance, should the results presented here be reproduced for other systems as well. These insights could help speed up the design of new antiagglomerants and guide future experiments.

TOC Graphic



Introduction

Gas hydrates are ice-like crystalline solids composed of polyhedral hydrogen-bonded water cages in which small gas molecules, *e.g.*, methane and carbon dioxide, are encapsulated. Gas hydrates are relevant for a variety of sectors, including energy, environment, and sustainability. With the goal of increasing the sustainability of our society, recent research advances have extended the utilization of gas hydrates in various applications, including but not limited to hydrogen and energy storage,¹⁻⁴ CO₂ capture and sequestration,⁵⁻⁷ water desalination,⁸⁻⁹ gas separation,¹⁰⁻¹¹ refrigeration and transport,¹² *etc.* Naturally occurring gas hydrates attract considerable attention for their potential role in providing an alternative energy source, as well as in environmental impacts.¹²⁻¹³ On the other hand, safety in the energy sector is frequently associated with the prevention of hydrate agglomeration in oil/gas pipelines.¹⁴ The formation, agglomeration and deposition of gas hydrates can cause flowline blockages, affecting deep-water drilling, oil/gas transport, and processing facilities, potentially leading to severe environmental and economic impacts.¹⁵⁻¹⁷

In this context, flow assurance activities are experiencing a remarkable change from “hydrate avoidance” to “hydrate management”, towards reducing capital and operational costs.¹⁸⁻²⁰ Hydrate inhibitors are commonly used to prevent the agglomeration of solid hydrate particles or their deposition on pipe walls. Depending on the expected inhibition mechanism, low-dosage hydrate inhibitors can be categorised as kinetic hydrate inhibitors (KHIs) and/or antiagglomerants (AAs).^{14-15, 21} KHIs and AAs can be effective at dosages in the range 0.5–2 vol%, while thermodynamic hydrate inhibitors require dosages of as high as 30–40 vol%.²¹⁻²³ However, the AA performance and their minimum effective dosage in specific applications vary, thereby affecting significantly the production costs. Although numerous studies have focused on understanding hydrate–hydrocarbon/water systems in the presence of AAs,²⁴⁻³³ many experimental^{28-29, 34} and computational³⁰⁻³² efforts are conducted at conditions somewhat far from those relevant in practice.

Insights regarding AA mechanisms of action have been obtained by measuring cohesive and adhesive forces.³⁵⁻³⁶ The MMF apparatus has shown great practical and fundamental potential, because it measures directly hydrate interparticle cohesive forces.^{23, 38-39} For example, Dieker *et al.*⁴⁰ and Aman *et al.*⁴¹

investigated the effect of carboxylic acids and crude oils on cyclopentane (CyC5) hydrate particle interactions. Assuming that capillary cohesion governs hydrate interparticle forces, the results suggest that surfactants could disturb the liquid bridge formed between hydrate particles, potentially reducing the cohesive forces.⁴⁰⁻⁴¹ Most previous studies were conducted using hydrates that are stable at atmospheric pressure, for example using hydrates of THF³⁷ and CyC5,^{23, 28, 38-39, 42-43} although the conditions are significantly different compared to those realistically experienced in typical flow assurance applications (high pressures and low temperatures). To probe realistic conditions, the High-Pressure Micromechanical Force Apparatus (HP-MMF)⁴⁴ was designed to quantify cohesive forces between ice particles and natural gas hydrate particles in both gas⁴⁴⁻⁴⁵ and liquid hydrocarbons.⁴⁶⁻⁴⁸ Recently, Koh et al.⁴⁸ employed the HP-MMF apparatus to measure CH₄/C₂H₆ hydrate cohesive forces in the presence of AAs. The flow assurance performance of those AAs was assessed using a rocking cell apparatus, as frequently done in industry. Comparing the datasets obtained, it was found that those AAs that substantially decrease the cohesive forces can show good overall performance in the rocking cell.⁴⁸ Of note, the molecular structure of the AAs used in these experiments was known, and in fact it had been used in prior atomistic molecular dynamics (MD) simulations by Striolo and his collaborators.^{31, 33, 49-50} Those simulations suggested that AAs that yield an ordered structure at the hydrate-oil interface can exhibit good practical performance. If MD simulations were consistent with HP-MMF experiments, then a seamless workflow could correlate AA molecular structure, their self-assembly at the hydrate-oil interface, their effect on hydrate-hydrate cohesive forces, and their macroscopic flow assurance performance, thereby providing a tool for the *in silico* design and screening of new potential AA molecules. The goal of this manuscript is to test whether such correlations are possible. While new MD simulation results are presented in this manuscript, the experimental data are taken from Koh et al.⁴⁸

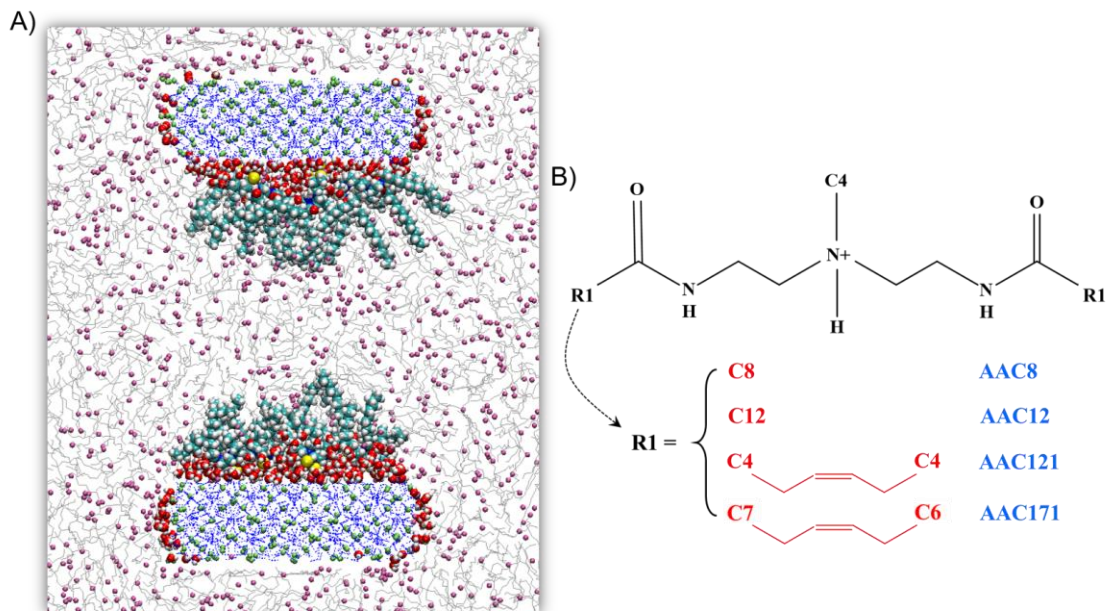


Figure 1. A) Representative simulation snapshot for the final configuration for a system composed of two sII hydrate particles covered with thin water films and AAs, immersed in a mixture of gaseous ($\text{CH}_4\text{-C}_2\text{H}_6$) and liquid hydrocarbons. Blue dotted lines symbolise water molecules in the hydrate. Purple and green spheres symbolise methane/ethane in the liquid and hydrate phases, respectively. Silver lines represent liquid hydrocarbons, *e.g.*, n-dodecane and n-heptane. Red and white spheres represent water oxygen and hydrogen atoms, respectively. Cyan, blue, red, white, and yellow spheres represent carbon, nitrogen, oxygen, hydrogen atoms in AA molecules, and chloride ions, respectively. B) Molecular structures of the AAs considered: AAC8 ($\text{R1} = \text{C8}$), AAC12 ($\text{R1} = \text{C12}$), AAC121 ($\text{R1} = \text{C4-C-C=C-C4}$), and AAC171 ($\text{R1} = \text{C7-C-C=C-C6}$).

Simulation Methodology

Model Setup. One representative simulation set up (see **Figure 1A**) mimics the measurements of hydrate particle cohesive forces conducted in experiments.⁴⁸ Each simulated system contains two hydrate nano-particles immersed in a hydrocarbon mixture. Each hydrate nano-particle was carved out of the bulk structure of sII $\text{CH}_4/\text{C}_2\text{H}_6$ hydrates⁵¹ which were used in the High-Pressure Micromechanical Force Apparatus (HP-MMF) and are expected to form within rocking cell experiments⁴⁸ to test the AA performance. The *X*, *Y* and *Z* dimensions of each hydrate nano-particle were 5.193, 3.462, and 1.731 nm, respectively. The hydrate substrates were parallel to the *X-Y* plane. On top of the hydrate particles, we deposited a thin water film with thickness of ~ 0.5 nm and a layer of quaternary ammonium surfactants AAs along the *Z*-direction.^{31, 42, 49-50} Thereafter, we duplicated the hydrate nano-particle covered with water and

AAs and placed the two hydrate nano-particles in a mirror-symmetric way along the Z-direction. The two hydrate nano-particles were then immersed in the hydrocarbon phase, yielding a simulation box length of 11.193, 3.462 and 16 nm in the X-, Y- and Z-directions, respectively. The hydrate substrates are infinite along the Y-direction due to the periodic boundary conditions applied in three directions.

In our simulations, the hydrocarbon phase contains either n-dodecane or n-heptane and CH₄/C₂H₆ gas mixtures with a molar ratio of 10:7.5:2.5. The gas mixture used in this study consists of 75 mol % of methane and 25 mol % of ethane, similar to the Green Canyon gases used in experiments.⁴⁸ The AAs considered are AAC8, AAC12, AAC121, AAC171 (their structures are shown in **Figure 1B**) at the AA surface density of 0.44 molecule/nm². The AAC171 was also simulated at the surface density of 0.28 molecule/nm², which in our approximation (based on the ratio of the reciprocals of two quantities, *e.g.*, the number of AA molecules and the molecular weight of AAs) corresponds to similar bulk AA concentration (in liquid hydrocarbons) as systems with AAC8, AAC12, and AAC121 at the surface density of 0.44 molecule/nm². It should be noted that experimental data are not available for the AAC121 surfactant, which was considered here, for illustration purposes, as a potential new AA, designed in silico. In **Table 1**, we report the compositions of the simulated systems.

Table 1. Compositions of the simulated systems.

	N _{CH₄-sII}	N _{C₂H₆-sII}	N _{H₂O-sII}	N _{H₂O}	N _{AAs}	N _{C₁₂:N_{CH₄:N_{C₂H₆}}}	N _{C₇:N_{CH₄:N_{C₂H₆}}}
AAs-0.44	216	72	1632	600	16	1160:870:290	1800:1350:450
AAC171-0.28	216	72	1632	600	10	1160:870:290	1800:1350:450

Force Fields and Implementation. Water molecules were represented by the TIP4P/Ice model,⁵² which has been proven successful to simulate hydrate nucleation and growth^{5,53} as well as to study the effectiveness of potential hydrate antiagglomerants.^{31, 49} AAs were modelled using the General Amber Force Field (GAFF),⁵⁴⁻⁵⁵ often employed to study organic and pharmaceutical molecules containing H, C, N, O, S, P, and halogens.⁵⁴

Hydrocarbons (*e.g.* methane, ethane, n-dodecane, and n-heptane) were described by implementing the united-atom version of the TraPPE-UA force field,⁵⁶ which accurately characterizes the vapor-liquid coexistence curves and critical properties of linear alkanes from methane to dodecane. We added chloride ions (Cl^-) represented as charged Lennard-Jones spheres⁵⁷ to maintain system charge neutrality. The chloride ions (Cl^-) were modelled using the potential parameters taken from Dang without polarizability,⁵⁷ because this force field is compatible with various water models.⁵⁸⁻⁵⁹ All non-bonded interactions were characterized by dispersion and electrostatic forces using the 12-6 Lennard-Jones (LJ) and Coulombic potentials, respectively. We employed the particle-particle particle-mesh (PPPM) method for treating long-range corrections⁶⁰ and the Lorentz-Berthelot combining rules to characterize the unlike LJ interactions.⁶¹ The cutoff distance of 14 Å was used for all interactions.

Equilibrium MD simulations were conducted using the GROMACS package,⁶² version 2016.3. We implemented simulation procedures similar to those used in our previous study.^{31, 49} First, we performed a NVT canonical ensemble simulation for 1 ns to relax the initial configuration while the hydrate layer was kept fixed. Subsequently, the simulations were carried out within the NPT ensemble under conditions similar to the experiments ($T = 274 \text{ K}$ and $P = 3.45 \text{ MPa}$) using Nose-Hoover thermostat and Berendsen/Parrinello-Rahman barostat.⁶² We implemented the pressure coupling only along the Z-direction, which enables us to keep X and Y dimensions of the simulation box constant. The equations of motion were solved using the leapfrog algorithm with the time step of 1.0 fs.⁶² We applied a harmonic restraint force ($k = 2000 \text{ kJ/mol.nm}$) on water, methane and ethane molecules in the two hydrate nanoparticles to tether them to their initial positions⁶² while other molecules in the system were allowed to move in the NPT simulations. We conducted each NPT simulation for $\geq 200 \text{ ns}$. To check whether the simulations reach equilibrium, we analyzed the convergence of system density and energy as well as density profiles of n-dodecane (or n-heptane) along the direction of the simulation box perpendicular to the hydrate particles.

Once equilibration was reached, we conducted umbrella-sampling (US) simulations⁶² to examine the interaction forces between the two hydrate nano-particles in the presence of various AAs, which have been investigated experimentally. The results from the US simulations were reconstructed to calculate the

Potential of Mean Force (PMF) experienced by the one hydrate nano-particle moving towards the other one along the Z-direction. The center of mass of the pulling hydrate particle was tethered by a harmonic spring of elastic constant 2000 kJ/mol.nm. During the US simulations, water, methane, and ethane molecules in the pulling hydrate particle were allowed to move freely while water–methane and water–ethane distances were constrained within the hydrate particles to maintain the sII hydrate structure. In each sampling window, an US run of 20 ns was conducted in the NVT ensemble. The Weighted Histogram Analysis Method (WHAM) algorithm was used to reconstruct the PMF profiles.⁶³ The bootstrap analysis employed in GROMACS was conducted to estimate the error bars.⁶³

Results and Discussion

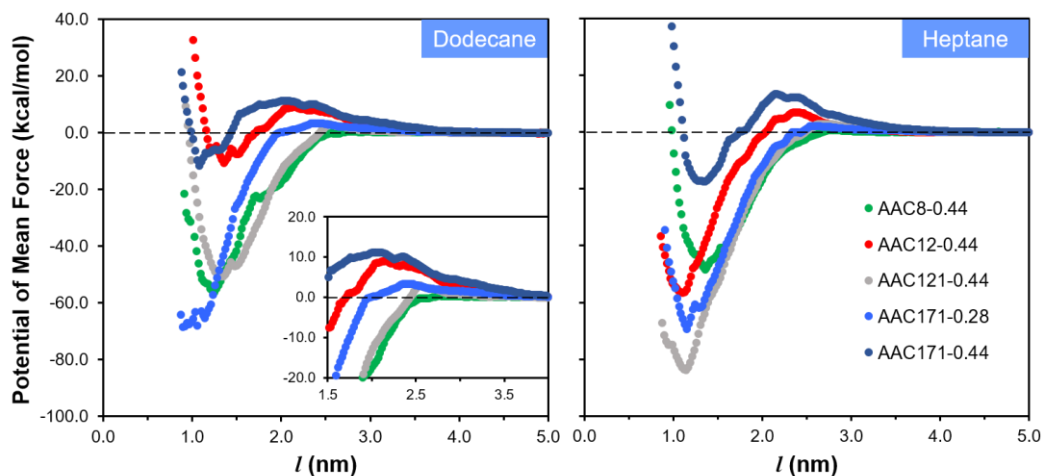


Figure 2. Potential of mean force profiles along the Z-direction (perpendicular to the hydrate surfaces) as experienced by one hydrate particle moving towards the other one in the presence of n-dodecane (left) and n-heptane (right). Results were obtained for the hydrate particles covered with AAC8 (green), AAC12 (red), AAC121 (grey), AAC171 (dark blue) at the surface density of 0.44 molecule/nm² and AAC171 at the surface density of 0.28 molecule/nm² (bright blue). The distance l is that between the planes formed by the water oxygen atoms of the surfaces of bottom and top hydrate nano-particles, which are in contact with thin water films and AAs.

Potential of Mean Force. In **Figure 2** we present the PMF profiles experienced by the two hydrate particles as they approach each other in the direction perpendicular to the hydrate-hydrocarbon interface. The results are shown for two liquid hydrocarbons: n-dodecane (left) and n-heptane (right). The PMF profiles were obtained as functions of the distance l between the surfaces of the two hydrates (see **Fig. 1A**).

The results depend strongly on the AAs used. Specifically, in the presence of AAC8 (green) the PMF profile shows an effective attraction between the two hydrate particles. On the other hand, the PMFs obtained in the presence of AAC12 (red), AAC121 (grey), and AAC171 (at both surface densities considered – dark and bright blue, respectively) show, as distance decreases, one repulsive barrier at intermediate l , a subsequent minimum, and a monotonic increase as l decreases. The repulsive barrier represents the work needed to compress and disperse the AA layers, which is dependent on the structural conformations of the AAs, *e.g.*, tail length, tail configurations (*e.g.*, inclusion of double bonds), packing density (AA surface density at 0.44 and 0.28 molecules/nm²), and the properties of solvents.⁶⁴ Much higher repulsive barriers are obtained in the presence of AAC12 (red) and AAC171 (dark blue), at the surface density of 0.44 molecule/nm², in both n-dodecane and n-heptane. Analysis of the density profiles for the AA films confined between the two hydrate particles when they are at a relative distance $l = 2.51$ nm, where the PMF shows a repulsive barrier for the system with AAC12, indicates a more pronounced density peak for the system with AAC12 compared to the results obtained the systems with AAC8 and AAC121 (as shown in **Figure S1** in the Supporting Information (SI)). One significant feature in the PMFs seems to strongly depend on the liquid hydrocarbon; specifically, the hydrates covered with AAC12 in n-heptane experience stronger attraction than those in n-dodecane when they begin to interact, whereas the interactions between the hydrates covered with AAC8 in n-dodecane are more attractive than those in n-heptane.

Varying AAs and the liquid hydrocarbon alters significantly the maximum distance at which the two hydrates experience an effective attraction (the PMF decreases below 0) (see **Table S1** in the SI). Specifically, effective attraction between two hydrate particles covered with AAs in both n-dodecane and n-heptane is felt at a distance l which increases in the following order: AAC171-0.44 < AAC12-0.44 < AAC171-0.28 < AAC121-0.44 < AAC8-0.44. The hydrate particles covered with AAC12, AAC121 and AAC171 in n-heptane seem to attract each other at distances further than when they are in n-dodecane. These results offer qualitative understanding of the dispersion behaviour of hydrate particles under the effect of various AAs and liquid HCs and provide some insights into the AA performance.

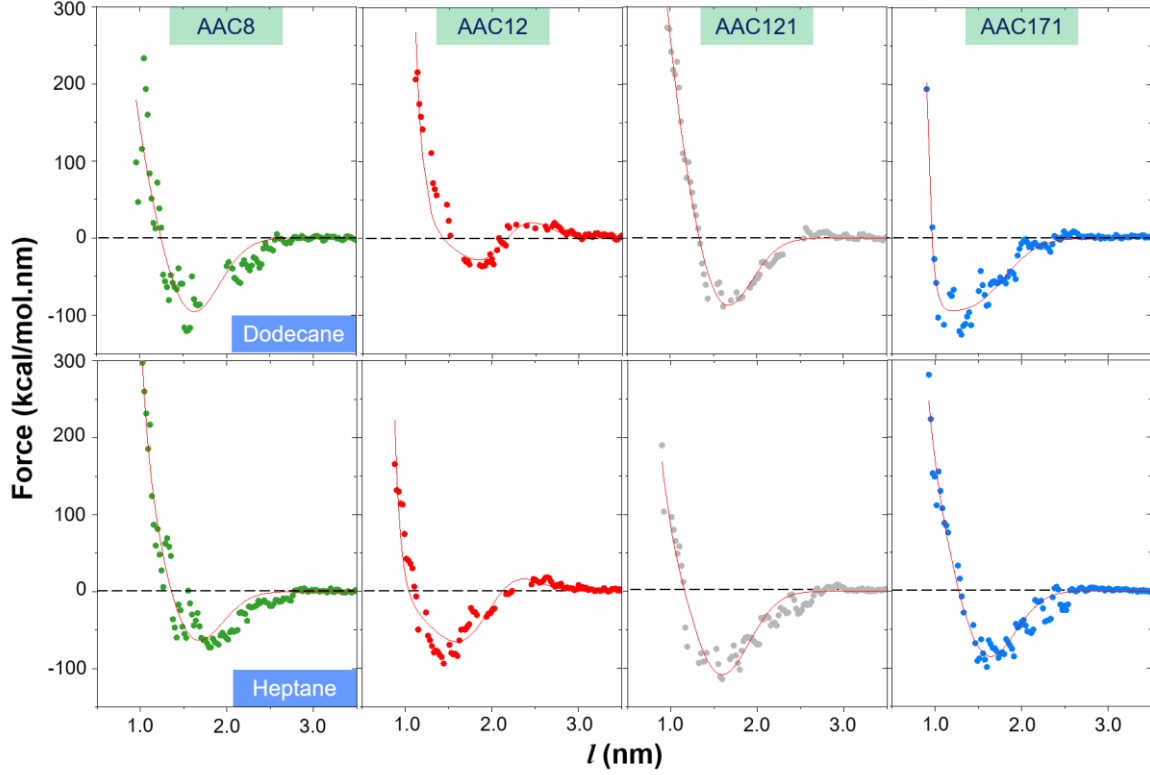


Figure 3. Simulated force–distance curves obtained for the hydrate particles in n-dodecane (top) and n-heptane (bottom). Red lines represent the fitting of data points to a mathematical function (Eq. (1)). Results were obtained for the hydrate particles covered with AAC8 (green), AAC12 (red), AAC121 (grey) at the surface density of 0.44 molecule/nm² and AAC171 at the surface density of 0.28 molecule/nm² (bright blue).

Force – Distance Profiles. By differentiation of the PMF profiles, we can obtain effective force–distance curves by $\langle F(l) \rangle = -dPMF(l)/dl$. The differentiation is conducted numerically by implementing a backward difference approximation. The resultant force–distance profiles are reminiscent of a Lennard-Jones force (with parameters ε and σ , which illustrate the depth of the attractive well and the distance at which the interaction potential is zero, respectively) superimposed to a repulsive force between the hydrate particles (with parameters r_o , b , and n , which control position and height of the repulsive peak), yielding the following expression:⁶⁵

$$F = 4\varepsilon \left(\frac{12\sigma^{12}}{r^{13}} - \frac{6\sigma^6}{r^7} \right) \times \left(1 - \sqrt{\pi} \exp \left[\frac{-(r-r_o)^2}{b} \right] \times n \right) \quad (1)$$

Fitting simulated force data points to Eq. (1) via adjusting the parameters ε , σ , r_o , b , and n (values reported in the SI) employing a non-linear regression with the Levenberg-Marquardt algorithm and removing outliers following the protocol suggested by Motulsky and Brown (details about the numerical procedure are described in the SI),⁶⁶ we observe that the force–distance profiles for the systems with AAC12 in the presence of n-dodecane and n-heptane (see **Figure 3**, top and bottom, respectively) present mid-range moderately repulsive peaks. These repulsions could prevent coalescence if strong enough, which is the aim of using AAs for hydrate management. The results present a different situation for the systems with AAC8 (green) as well as AAC121 (grey) and AAC171 at AA surface density of 0.28 molecule/nm² (bright blue) in n-dodecane (**Fig. 3**, top) and n-heptane (**Fig. 3**, bottom). For these systems, the force profiles are consistent with an effective attraction between the two hydrates, even in the presence of the AAs. These simulation results suggest that AAC12 might exhibit good anti-agglomerant performance in n-dodecane and n-heptane compared to the other AAs at the same vol% in the hydrocarbon phase. These expectations are indeed qualitatively consistent with experimental observations.⁴⁸

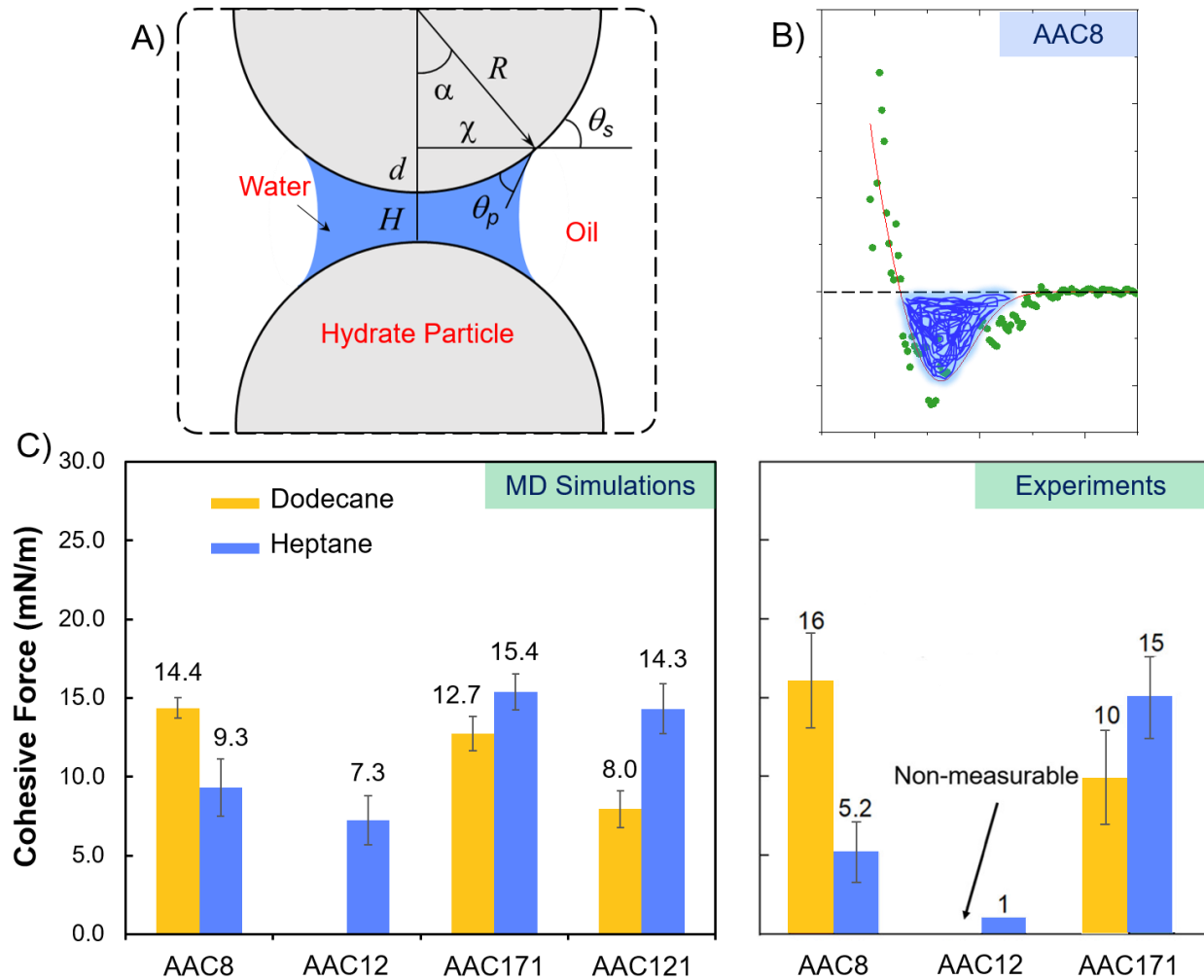


Figure 4. A) Schematic of particle–particle capillary cohesion with parameters: particle radius (R), particle separation distance (H), liquid bridge immersion depth (d), capillary bridge width (χ), embracing angle (α), external contact angle (θ_s), and contact angle (θ_p), adapted from Aman et al.³⁸ B) Schematic of the calculation for cohesive work attributed to hydrate-hydrate cohesion (blue shaded region under the line of zero-value of force). C) Experimental and simulated cohesive force data between two hydrate particles covered with AAs immersed in n-dodecane (yellow) and n-heptane (blue). Simulation results were obtained in the presence of AAC8, AAC12, AAC121 at the surface density of 0.44 molecule/nm² and AAC171 at the surface density of 0.28 molecule/nm². Results from MD simulations (left, this work) and HP-MMF experiments (right, adapted from Koh et al.⁴⁸) are shown. In the experimental data, the surface density of AAs is not known, although all experiments were conducted at the AA concentration of 0.5 vol %. Pressure and temperature conditions considered in the experiments are the same as those used in the simulations: 3.45 MPa and 274 K.

Hydrate Particle Cohesive Forces. To quantitatively compare the simulation results with the experimental data reported by Koh et al.,⁴⁸ we quantify the cohesive force. The hydrate interparticle cohesive force measurements are interpreted using the capillary bridge theory.^{67-68 69 36}

$$\frac{F_A}{R^*} = 2\pi\gamma\sin(\alpha)\sin(\theta_p + \theta_s) + \frac{2\pi\gamma\cos\theta_p}{1+H/2d} \quad (2)$$

In Eq. (2), F_A is the hydrate interparticle cohesive force, R^* is the harmonic mean radius of the particle pair, and other relevant parameters are described in **Figure 4A**.

Assuming that the pressure difference between the bulk phases and the bridge (capillary pressure) is extremely small for the systems considered in the current investigation, the cohesive force between two nano-particles can be described by the following expression, where the first term of Eq. (2) is modified to take into account only the particle–particle contact area and the second term of Eq. (2) is removed.³⁸

$$\frac{F}{L^*} = \frac{W_{sep}}{A} \quad (3)$$

In Eq. (3), F is hydrate–hydrate cohesive force, W_{sep} is work of separation of two hydrate nano-particles or also the hydrate-hydrate cohesive work (illustrated as blue shaded region in **Figure 4B**), L^* is the harmonic mean circumference of the hydrate particle pair, and A is the surface area of the interface.

Table 2. Work of cohesion for the systems with AAC8, AAC12, AAC121 at the AA surface density of 0.44 molecule/nm² and AAC171 at AA surface density of 0.28 molecule/nm² in the presence of n-dodecane and n-heptane.

	Work of Cohesion (kcal/mol)	
	n-dodecane	n-heptane
AAC8 – 0.44	74.35 ± 3.40	48.23 ± 9.44
AAC12 – 0.44	-2.58 ± -0.70	37.54 ± 8.08
AAC121 – 0.44	41.14 ± 6.06	74.15 ± 8.18
AAC171 – 0.28	65.94 ± 5.57	79.61 ± 5.88

In **Table 2**, we report the work of cohesion W_{sep} for the systems with AAC8, AAC12, AAC121 at the AA surface density of 0.44 molecule/nm² and AAC171 at AA surface density of 0.28 molecule/nm² in the presence of n-dodecane and n-heptane. W_{sep} is determined by the integration of the force–distance curves under the reference line at $F = 0$ until the force approaches the zero value.⁷⁰ The results show negative W_{sep} only for the case in which the two hydrate nano-particles covered with AAC12 in n-dodecane are brought closer together. This suggests that the cohesive force measurement for this system is inaccessible, which shows excellent agreement with the recent experimental observation.⁴⁸ On the other hand, we observe positive values of W_{sep} for all the other systems.

When values for the work of cohesion are known, we further quantify the cohesive force (F/L^*) in Eq. (4). In **Figure 4C**, left, we show the cohesive force calculated for the systems with AAC8, AAC12, AAC121 at the surface density of 0.44 molecule/nm² and AAC171 at the surface density of 0.28 molecule/nm² in n-dodecane and n-heptane. The cohesive force found in the presence of AAC8 in n-dodecane is larger than that obtained in n-heptane, suggesting that AAC8 performs better as an AA in the latter than in the former hydrocarbon, whereas the results obtained for AAC12, AAC121 and AAC171 show the opposite trends. Our previous MD study also suggested that AAC12 might perform better in n-dodecane than in n-octane and in n-hexane.³¹ Because our simulation results are quantitatively comparable to experimental measurements (see **Figure 4C**, right),⁴⁸ we propose that the simulation protocol implemented here could be used to predict AA performance. For example, the AAC121 surfactant was not considered in the experimental campaign reported by Koh et al.⁴⁸ The MD results presented in **Fig. 4C** suggest that this molecule might not be a good AA candidate in either liquid hydrocarbon for use in flow assurance, as it yields measurable and rather high cohesive forces between the hydrates.

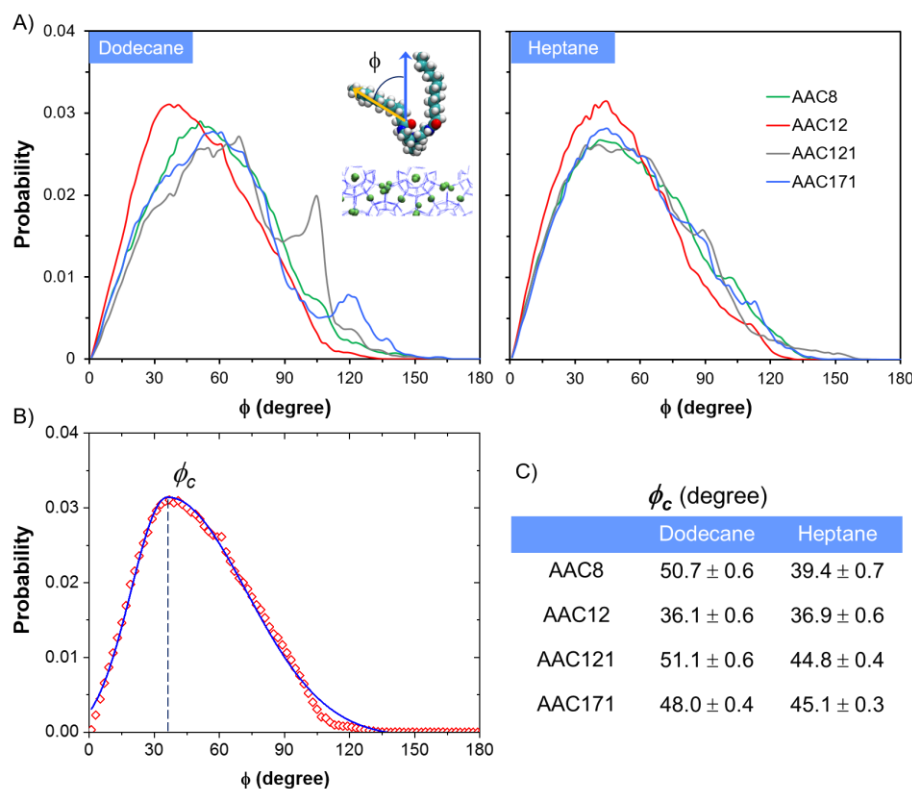


Figure 5. A) Probability distributions of orientational angle ϕ for AAC8 (green), AAC12 (red), AAC121 (grey) at 0.44 molecule/nm² and AAC171 at 0.28 molecule/nm² (bright blue). Results were obtained in n-dodecane (left) and n-heptane (right). The inset in the left panel shows a diagram describing the orientational angle ϕ formed by the vector connecting the first to the last carbon atoms of the AA long tails and the direction perpendicular to the hydrate surface. B) Fitting data points of the probability distribution of the orientational angle with a skew-Gaussian curve. C) The global maximum of the Gaussian hills ϕ_c obtained from fitting the probability distribution of the orientational angle for all systems considered.

AA Orientation. In an attempt to identify molecular features that correlate with the cohesive force data shown in **Fig. 4C**, we examine the orientation of AAs adsorbed on the hydrate surfaces. Previous studies suggested that the orientational ordering of AAs could help predict AAs performance in hydrate management (the more uprightly AAs orient, the better they perform),^{31, 71} as a well-ordered AA film can effectively exclude CH₄/C₂H₆ from the interfacial layer, which possibly hinders hydrate growth.^{31, 50} To quantify the AA orientation, we calculate the probability distribution of the orientational angle ϕ formed between each surfactant tail and the surface normal, *e.g.* Z-direction. For all AAs, we observe wide probability distributions at the low AA surface densities considered here (see **Figure 5A**), consistent with previous results.^{31, 33} These results suggest that the AAs remain orientationally disordered at the conditions

probed in the present study. Fitting the probability distributions with skew-Gaussian curves (see **Figure 5B**), we obtained the global maximum of the Gaussian hills ϕ_c for all systems considered (see **Figure 5C**). The ϕ_c for AAC8 in n-heptane (39°) is smaller than in n-dodecane (51°), which means AAC8 molecules orient their long hydrocarbon tails more vertically in n-heptane than in n-dodecane, possibly explaining why AAC8 yields larger cohesive force in n-dodecane than in n-heptane. Nevertheless, the ϕ_c for other AAs considered here do not correlate with the corresponding cohesive forces. For example, the ϕ_c for AAC12 in both liquid hydrocarbons are rather comparable (36° – 37°) despite the fact that AAC12 shows much better performance in n-dodecane. This suggests that, although the interfacial orientation might be important in explaining the AAs performance at high AA surface densities, it might not be sufficient to explain cohesive energy data. Other mechanisms are likely affecting AAs performance.

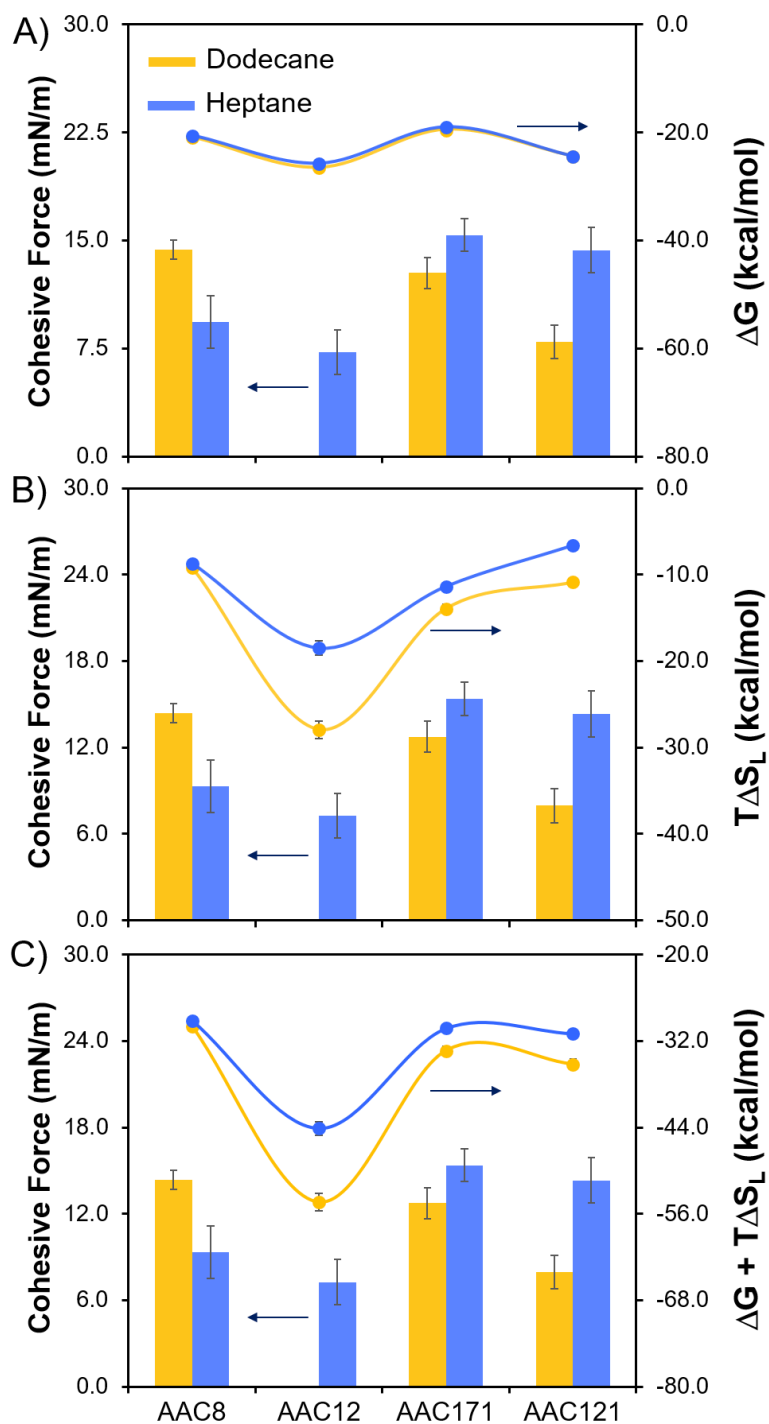


Figure 6. Simulated cohesive force (bars) between two hydrate particles covered with AAs immersed in n-dodecane (yellow) and n-heptane (blue) with free energy (panel A), entropy change (panel B) and sum of free energy and entropy change (panel C) associated with solvation of AA molecules in the presence of n-dodecane and n-heptane (yellow and blue, filled circles, respectively) at 274 K and 3.45 MPa. The computational results were obtained for the systems with AAC8, AAC12, AAC121 and AAC171.

Free Energy and Entropy Changes on Solvation of AAs. To determine which other molecular factors might affect the effectiveness of AAs in hydrate management, we recall the suggestion that hydrocarbons provide more favourable solvation free energy to longer hydrophobic AAs tails.²⁶ Using the perturbation method coupled with the Bennett acceptance ratio protocol,⁶² we analysed the free energy changes upon solvation of the AAC8, AAC12, AAC12 at 0.44 molecule/nm² and AAC171 at 0.28 molecule/nm² in both n-dodecane (yellow) and n-heptane (blue), as shown in **Figure 6A**, filled circles. The results show the AA solvation free energies computed in both liquid hydrocarbons are similar, although the corresponding cohesive forces are rather different (columns shown in **Figure 6A**). The solvation free energy of AAC12 is also comparable to that of AAC121 in n-dodecane and n-heptane, possibly because these surfactants have the same tail length, despite the fact that AAC12 shows much better performance than AAC121. Therefore, we conclude that solvation free energy alone cannot explain the correlation between simulated and experimental data presented here, regarding AA flow assurance performance.

Because of the significant contribution of the entropy coupled with the conformational degrees of freedom to the thermodynamics of solvation of molecules,⁷²⁻⁷³ we computed the configurational entropy, S_L , of AAs in liquid hydrocarbons via the method developed by Schlitter and others.⁷⁴⁻⁷⁷ Note that the configurational entropy corresponds to the entropy associated with the intramolecular vibrations of a molecule⁷⁸ and thus analysis of configurational entropy of a molecule will provide insights into the degree of its flexibility.⁷⁹⁻⁸⁰ S_L is quantified by calculating the covariance of the Cartesian coordinates of atoms of one AA molecule with the following expression:⁷²

$$S_L = \frac{1}{2} k \ln \det \left[1 + \frac{kT e^2}{\hbar} M^{1/2} \sigma M^{1/2} \right] \quad . \quad (4)$$

In Eq. (4), M is the $3N$ -dimensional diagonal mass matrix for one AA of N atoms; σ is the covariance in positions of the AA atoms; e is the Euler number; T is the simulation temperature; and k is the Boltzmann constant. The entropy change because of the reorganization of AAs in the presence of solvent at density ρ can be estimated as $\Delta S_L = S_L(\rho) - S_L(\rho = 0)$.

We report the entropy change $T\Delta S_L$ (as shown in **Fig. 6B**, filled circles) associated with solvation of AAC8, AAC12, AAC121 at 0.44 molecule/nm² and AAC171 at 0.28 molecule/nm² in n-dodecane (yellow) and n-heptane (blue) at 274 K and 3.45 MPa. Note that the larger the entropy change upon solvation is, the more inflexible the AAs become when dissolved in the hydrocarbons, perhaps suggesting higher efficiency in preventing CH₄/C₂H₆ from entering the interfacial layer. The results show that $T\Delta S_L$ for AAC12, AAC171 and AAC121 in n-dodecane are larger than the corresponding values in n-heptane, suggesting that the AAs considered here are less flexible in n-dodecane than in n-heptane, which possibly explains why the cohesive forces between two hydrate particles measured are smaller in n-dodecane. Contrarily, while $T\Delta S_L$ for AAC171 in both liquid hydrocarbons are larger than the results obtained for AAC121, the cohesive forces between two hydrate particles covered with AAC171 are greater. In addition, $T\Delta S_L$ for AAC171 in n-heptane is higher than that calculated for AAC8, albeit the cohesive forces between two hydrate particles covered with AAC171 in n-heptane are larger. Thus, our results suggest no correlation between the entropy change upon solvation of AAs and their flow assurance performance, at least within our dataset.

However, combining free energy and entropy changes associated with solvation of AAs, which represents the enthalpy of solvation ($\Delta G + T\Delta S_L$), we observe a direct correlation with AA performance, i.e., $\Delta G + T\Delta S_L$ data for AAs in n-dodecane follow the order: AAC12 > AAC121 > AAC171 > AAC8, which is consistent with the order obtained for the cohesive forces (see **Fig. 6C**). To support our results, we note that Lynden-Bell et al.⁸¹ previously identified a correlation between the solvation free energy of a non-polar molecule and its hydration structure. We note that $\Delta G + T\Delta S_L$ for AAC8 in n-heptane is comparable to values calculated for AAC171 and AAC121 ($\sim -30.1 \pm 0.6$ kcal/mol), although AAC8, AAC171 and AAC121 in n-heptane show significant differences in orientation (see **Fig. 5C**). Similarly, $\Delta G + T\Delta S_L$ values for AAC8 in the two hydrocarbons considered here are equivalent, while the respective molecular orientation is different. This suggests that, when $\Delta G + T\Delta S_L$ values predicted for two AAs are similar, the AA orientation at the hydrate-hydrocarbon interface might correlate with macroscopic performance. Comparing the results obtained for AAC171 and AAC121, we conclude that including one double bond in

the tails of these AAs increases their degree of flexibility and thereby reduces their effectiveness in preventing hydrate agglomeration. These observations suggest that the quantification of $\Delta G + T\Delta S_L$ changes on solvation of AA coupled with the AA orientation at hydrate-oil interface, as well as with cohesion force between hydrate particles could be used to predict AA performance. Certainly, more extensive datasets should be used to test whether this correlation has predictive capabilities.

One might wonder why AAC12 molecules orient their n-dodecyl tails more uprightly and become less flexible in n-dodecane than in n-heptane compared to the other AAs (see **Fig. 5**). Employing neutron and X-ray diffraction techniques, Clarke and his coworkers⁸² found out that dodecane forms additional phases with parallel and upright molecular structures, even at high temperature (290 K), at both low and high coverages, as opposed to other hydrocarbons. This could help us understand previous observations according to which mixtures of surfactants with n-dodecyl tails with dodecane could yield ordered interfacial monolayers, while ordered interfacial films could not be observed for mixed n-octyl-octane³¹ or n-hexyl-hexane⁸³ monolayers.

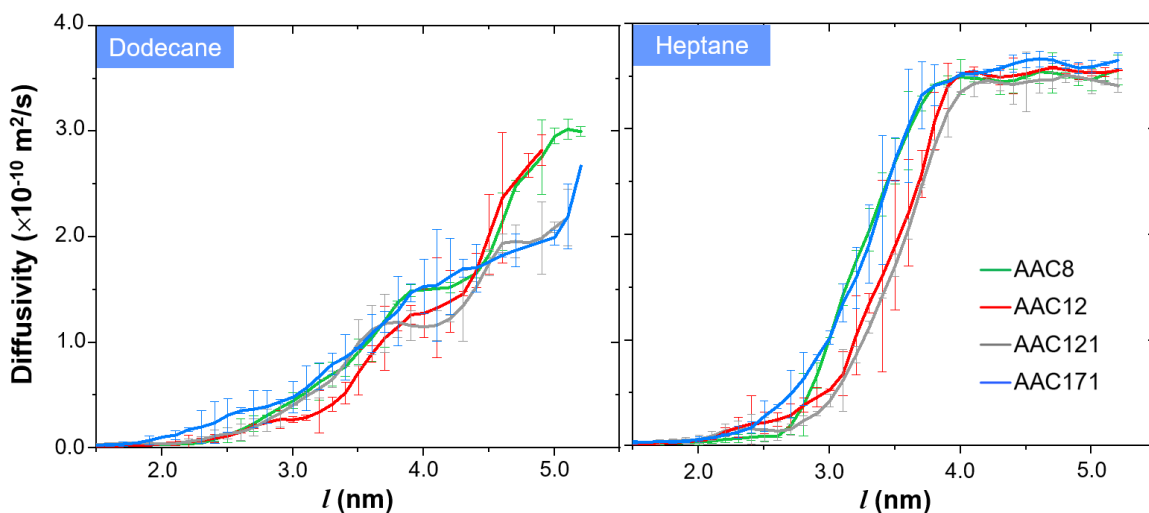


Figure 7. Diffusion profiles along the Z-direction for one hydrate particle moving towards the other one in the presence of n-dodecane (left) and n-heptane (right). Results were obtained for the systems in the presence of AAC8 (green), AAC12 (red), AAC121 (grey) at the AA surface density of 0.44 molecule/nm² and AAC171 at AA surface density of 0.28 molecule/nm² (bright blue). Each line represents the diffusion profile for a hydrate particle with one AA obtained by smoothing data points of diffusivity using adjacent-averaging filter.

Dynamic Properties. To complement the thermodynamic analysis, we estimated the position-dependent diffusion profiles, thereby obtaining molecular-level understanding of the transport of hydrate particles covered with AAs across the hydrocarbon phase. The variation of the hydrate particle diffusivity can be affected by variation of the frictional environment as the particle moves from the bulk hydrocarbon phase towards the other particle. Due to the heterogeneity of simulated systems, the calculation of position-dependent diffusion constant is more reliable than the quantification of mean square displacements.⁸⁴ It is worth noting that the ability to suspend/disperse hydrate particles in a liquid hydrocarbon phase is important for hydrate slurry transport. We extended the standard scope of the US framework considering the method originated by Straub et al.⁸⁵ and elaborated by Hummer,⁸⁶ where the position-dependent diffusion coefficient is calculated from the position autocorrelation function (PACF) obtained from harmonically restrained simulations:^{32, 71, 87}

$$D(z_k = \langle z \rangle_k) = \frac{\text{var}(z)^2}{\int_0^\infty C_{zz}(t) dt} \quad (5)$$

In Eq. (5), $\langle z \rangle_k$ is the average of the Cartesian position of the hydrate particle along the Z-direction in the US window k , $C_{zz}(t) = \langle \delta z(0) \delta z(t) \rangle$ the PACF calculated directly from the time series, and $\text{var}(z) = \langle z^2 \rangle - \langle z \rangle^2$ is its variance.

Our results, in **Figure 7**, show that the hydrocarbon phase strongly affects the diffusion profiles of the hydrate particles. In particular, the hydrate particles diffuse in bulk n-heptane ($\sim 3.5 \times 10^{-10}$ m²/s) faster than in n-dodecane ($\sim 3.0 \times 10^{-10}$ m²/s), probably due to the smaller viscosity of n-heptane. Varying AAs moderately alters the diffusion of the hydrate particles. Specifically, the diffusivities of the hydrate particles covered with AAC12 and AAC121 in n-heptane are smaller than those obtained for AAC8 and AAC171 when the two hydrate particles start approaching each other. While these results could be useful for modelling of transport of hydrate particles at large length scales, they do not seem to be strongly correlated with the performance of the AAs.

Conclusions

Employing classic molecular dynamics simulations, we investigated the interactions between gas hydrate nano-particles immersed in hydrocarbons in the presence of AAs under industrially relevant conditions, and we correlated the results with the performance of the AAs for hydrate management. The simulated results of hydrate particle cohesive forces for the systems with AAC8, AAC12 and AAC171 in n-dodecane and n-heptane are quantitatively comparable to those measured from HP-MMF experiments. Excellent agreement between simulated and HP-MMF experimental data suggests that a practical workflow might be possible to predict the performance of AAs. Further, our simulation results reveal, for the first time, some of the key factors that might determine the performance of AAs for the prevention of hydrate agglomeration. These include the orientation of AAs adsorbed at the hydrate-oil interface as well as free energy and entropy changes associated with solvation of AAs, the latter indicating the degree of AAs molecular flexibility upon AA solvation. Our analysis not only explain why the liquid hydrocarbons can affect the AA performance, but, once extended to other relevant systems, could provide a workflow for the accelerated design of new antiagglomerants.

Acknowledgments

Financial support was generously provided, in part, by the UK EPSRC, under grant number EP/T004282/1, and by the US National Science Foundation, under grant number CBET 2015201 (CAK). Generous allocations of computing time were provided by ARCHER, the UK National Supercomputing Service (<http://www.archer.ac.uk>) and by the University College London Research Computing Platforms Support (Young).

Supporting Information

The Supporting Information is available free of charge on the ACS Publications website. Numerical details on fitting simulated force data and results for properties such as density profiles of antiagglomerant molecules between two hydrate particles, locations of minimum and local maxima in the PMF profiles, locations where attraction initiates, and fitting parameters for force – distance curves.

References

1. Sugahara, T.; Haag, J. C.; Prasad, P. S. R.; Warntjes, A. A.; Sloan, E. D.; Sum, A. K.; Koh, C. A. Increasing Hydrogen Storage Capacity Using Tetrahydrofuran. *J Am Chem Soc* **2009**, *131*, 14616-+.
2. Koh, D. Y.; Kang, H.; Jeon, J.; Ahn, Y. H.; Park, Y.; Kim, H.; Lee, H. Tuning Cage Dimension in Clathrate Hydrates for Hydrogen Multiple Occupancy. *J Phys Chem C* **2014**, *118*, 3324-3330.
3. Denning, S.; Majid, A. A. A.; Lucero, J. M.; Crawford, J. M.; Carreon, M. A.; Koh, C. A. Metal-Organic Framework Hkust-1 Promotes Methane Hydrate Formation for Improved Gas Storage Capacity. *Acs Appl Mater Inter* **2020**, *12*, 53510-53518.
4. Khurana, M.; Veluswamy, H. P.; Daraboina, N.; Linga, P. Thermodynamic and Kinetic Modelling of Mixed CH₄-THF Hydrate for Methane Storage Application. *Chem Eng J* **2019**, *370*, 760-771.
5. Phan, A.; Schlösser, H.; Striolo, A. Molecular Mechanisms by Which Tetrahydrofuran Affects CO₂ Hydrate Growth: Implications for Carbon Storage. *Chem Eng J* **2021**, *418*, 129423.
6. Lee, D.; Lee, Y.; Lim, J.; Seo, Y. Guest Enclathration and Structural Transition in CO₂ + N₂ + Methylcyclopentane Hydrates and Their Significance for CO₂ Capture and Sequestration. *Chem Eng J* **2017**, *320*, 43-49.
7. Moon, S.; Ahn, Y. H.; Kim, H.; Hong, S.; Koh, D. Y.; Park, Y. Secondary Gaseous Guest-Dependent Structures of Binary Neopentyl Alcohol Hydrates and Their Tuning Behavior for Potential Application to CO₂ Capture. *Chem Eng J* **2017**, *330*, 890-898.
8. Babu, P.; Nambiar, A.; He, T. B.; Karimi, I. A.; Lee, J. D.; Englezos, P.; Linga, P. A Review of Clathrate Hydrate Based Desalination to Strengthen Energy-Water Nexus. *Acs Sustain Chem Eng* **2018**, *6*, 8093-8107.
9. Seo, S. D.; Hong, S. Y.; Sum, A. K.; Lee, K. H.; Lee, J. D.; Lee, B. R. Thermodynamic and Kinetic Analysis of Gas Hydrates for Desalination of Saturated Salinity Water. *Chem Eng J* **2019**, *370*, 980-987.
10. Kumar, R.; Englezos, P.; Moudrakovski, I.; Ripmeester, J. A. Structure and Composition of CO₂/H₂ and CO₂/H₂/C₃H₈ Hydrate in Relation to Simultaneous CO₂ Capture and H₂ Production. *Aiche J* **2009**, *55*, 1584-1594.
11. Papadimitriou, N. I.; Tsimpanogiannis, I. N.; Economou, I. G.; Stubos, A. K. Monte Carlo Simulations of the Separation of a Binary Gas Mixture (CH₄ + CO₂) Using Hydrates. *Phys Chem Chem Phys* **2018**, *20*, 28026-28038.
12. Hassanpouryouzband, A.; Joonaki, E.; Farahani, M. V.; Takeya, S.; Ruppel, C.; Yang, J. H.; English, N. J.; Schicks, J. M.; Edlmann, K.; Mehrabian, H.; Aman, Z. M.; Tohidi, B. Gas Hydrates in Sustainable Chemistry. *Chem Soc Rev* **2020**, *49*, 5225-5309.
13. Fu, X. J.; Jimenez-Martinez, J.; Nguyen, T. P.; Carey, J. W.; Viswanathan, H.; Cueto-Felgueroso, L.; Juanes, R. Crustal Fingering Facilitates Free-Gas Methane Migration through the Hydrate Stability Zone. *P Natl Acad Sci USA* **2020**, *117*, 31660-31664.
14. Striolo, A.; Phan, A.; Walsh, M. R. Molecular Properties of Interfaces Relevant for Clathrate Hydrate Agglomeration. *Curr Opin Chem Eng* **2019**, *25*, 57-66.
15. Kelland, M. A., *Production Chemicals for the Oil and Gas Industry*; CRC Press, 2010; Vol. 72.
16. Dendy Sloan, E.; Koh, C. A., *Clathrate Hydrates of Natural Gases*, 3rd ed. ed.; CRC Press - Taylor & Francis Group, 2007, p 752.
17. Dendy Sloan, E.; Koh, C. A.; Sum, A., *Natural Gas Hydrates in Flow Assurance*; Elsevier: Boston, 2011.
18. Kinnari, K.; Hundseid, J.; Li, X. Y.; Askvik, K. M. Hydrate Management in Practice. *J Chem Eng Data* **2015**, *60*, 437-446.
19. Rao, I.; Koh, C. A.; Sloan, E. D.; Sum, A. K. Gas Hydrate Deposition on a Cold Surface in Water-Saturated Gas Systems. *Ind Eng Chem Res* **2013**, *52*, 6262-6269.
20. Dapena, J. A.; Majid, A. A.; Srivastava, V.; Wang, Y.; Charlton, T. B.; Gardner, A. A.; Sloan, E. D.; Zerpa, L. E.; Wu, D. T.; Koh, C. A., Gas Hydrate Management Strategies Using Anti-Agglomerants:

Continuous & Transient Large-Scale Flowloop Studies. In *Offshore Technology Conference*, Offshore Technology Conference: Houston, Texas, USA,, 2017; p 16.

21. Kelland, M. A. History of the Development of Low Dosage Hydrate Inhibitors. *Energ Fuel* **2006**, *20*, 825-847.
22. Perrin, A.; Musa, O. M.; Steed, J. W. The Chemistry of Low Dosage Clathrate Hydrate Inhibitors. *Chem Soc Rev* **2013**, *42*, 1996-2015.
23. Aman, Z. M.; Olcott, K.; Pfeiffer, K.; Sloan, E. D.; Sum, A. K.; Koh, C. A. Surfactant Adsorption and Interfacial Tension Investigations on Cyclopentane Hydrate. *Langmuir* **2013**, *29*, 2676-2682.
24. Li, S. X.; Lv, R. J.; Yan, Z. S.; Huang, F.; Zhang, X. R.; Chen, G. J.; Yue, T. T. Design of Alanine-Rich Short Peptides as a Green Alternative of Gas Hydrate Inhibitors: Dual Methyl Group Docking for Efficient Adsorption on the Surface of Gas Hydrates. *ACS Sustain Chem Eng* **2020**, *8*, 4256-4266.
25. Jimenez-Angeles, F.; Firoozabadi, A. Hydrophobic Hydration and the Effect of NaCl Salt in the Adsorption of Hydrocarbons and Surfactants on Clathrate Hydrates. *ACS Central Sci* **2018**, *4*, 820-831.
26. Mehrabian, H.; Walsh, M. R.; Trout, B. L. In Silico Analysis of the Effect of Alkyl Tail Length on Antiagglomerant Adsorption to Natural Gas Hydrates in Brine. *J Phys Chem C* **2019**, *123*, 17239-17248.
27. Mehrabian, H.; Trout, B. L. In Silico Engineering of Hydrate Anti-Agglomerant Molecules Using Bias-Exchange Metadynamics Simulations. *J Phys Chem C* **2020**, *124*, 18983-18992.
28. Brown, E. P.; Koh, C. A. Competitive Interfacial Effects of Surfactant Chemicals on Clathrate Hydrate Particle Cohesion. *Energ Fuel* **2016**, *30*, 8065-8071.
29. Chua, P. C.; Kelland, M. A. Study of the Gas Hydrate Antiagglomerant Performance of a Series of Mono- and Bis-Amine Oxides: Dual Antiagglomerant and Kinetic Hydrate Inhibition Behavior. *Energ Fuel* **2018**, *32*, 1674-1684.
30. Bellucci, M. A.; Walsh, M. R.; Trout, B. L. Molecular Dynamics Analysis of Anti-Agglomerant Surface Adsorption in Natural Gas Hydrates. *J Phys Chem C* **2018**, *122*, 2673-2683.
31. Bui, T.; Phan, A.; Monteiro, D.; Lan, Q.; Ceglie, M.; Acosta, E.; Krishnamurthy, P.; Striolo, A. Evidence of Structure-Performance Relation for Surfactants Used as Antiagglomerants for Hydrate Management. *Langmuir* **2017**, *33*, 2263-2274.
32. Phan, A.; Bui, T.; Acosta, E.; Krishnamurthy, P.; Striolo, A. Molecular Mechanisms Responsible for Hydrate Anti-Agglomerant Performance. *Phys Chem Chem Phys* **2016**, *18*, 24859-24871.
33. Bui, T.; Sicard, F.; Monteiro, D.; Lan, Q.; Ceglie, M.; Burrell, C.; Striolo, A. Antiagglomerants Affect Gas Hydrate Growth. *J Phys Chem Lett* **2018**, *9*, 3491-3496.
34. Chua, P. C.; Kelland, M. A. Study of the Gas Hydrate Anti-Agglomerant Performance of a Series of N-Alkyl-Tri(N-Butyl)Ammonium Bromides. *Energ Fuel* **2013**, *27*, 1285-1292.
35. Wang, W. C.; Li, Y. X.; Liu, H. H.; Zhao, P. F. Study of Agglomeration Characteristics of Hydrate Particles in Oil/Gas Pipelines. *Adv Mech Eng* **2015**, *7*, 457050.
36. Israelachvili, J. N., *Intermolecular and Surface Forces*, 2nd edition ed. ed.: Academic Press, 1991.
37. Yang, S. O.; Kleehammer, D. M.; Huo, Z. X.; Sloan, E. D.; Miller, K. T. Temperature Dependence of Particle-Particle Adherence Forces in Ice and Clathrate Hydrates. *J Colloid Interf Sci* **2004**, *277*, 335-341.
38. Aman, Z. M.; Joshi, S. E.; Sloan, E. D.; Sum, A. K.; Koh, C. A. Micromechanical Cohesion Force Measurements to Determine Cyclopentane Hydrate Interfacial Properties. *J Colloid Interf Sci* **2012**, *376*, 283-288.
39. Brown, E. P.; Hu, S. J.; Wells, J.; Wang, X. H.; Koh, C. A. Direct Measurements of Contact Angles on Cyclopentane Hydrates. *Energ Fuel* **2018**, *32*, 6619-6626.
40. Dieker, L. E.; Aman, Z. M.; George, N. C.; Sum, A. K.; Sloan, E. D.; Koh, C. A. Micromechanical Adhesion Force Measurements between Hydrate Particles in Hydrocarbon Oils and Their Modifications. *Energ Fuel* **2009**, *23*, 5966-5971.

41. Aman, Z. M.; Dieker, L. E.; Aspenes, G.; Sum, A. K.; Sloan, E. D.; Koh, C. A. Influence of Model Oil with Surfactants and Amphiphilic Polymers on Cyclopentane Hydrate Adhesion Forces. *Energ Fuel* **2010**, *24*, 5441-5445.
42. Aman, Z. M.; Brown, E. P.; Sloan, E. D.; Sum, A. K.; Koh, C. A. Interfacial Mechanisms Governing Cyclopentane Clathrate Hydrate Adhesion/Cohesion. *Phys Chem Chem Phys* **2011**, *13*, 19796-19806.
43. Aspenes, G.; Dieker, L. E.; Aman, Z. M.; Hoiland, S.; Sum, A. K.; Koh, C. A.; Sloan, E. D. Adhesion Force between Cyclopentane Hydrates and Solid Surface Materials. *J Colloid Interf Sci* **2010**, *343*, 529-536.
44. Lee, B. R.; Sum, A. K. Micromechanical Cohesion Force between Gas Hydrate Particles Measured under High Pressure and Low Temperature Conditions. *Langmuir* **2015**, *31*, 3884-3888.
45. Wang, S. L.; Hu, S. J.; Brown, E. P.; Nakatsuka, M. A.; Zhao, J. F.; Yang, M. J.; Song, Y. C.; Koh, C. A. High Pressure Micromechanical Force Measurements of the Effects of Surface Corrosion and Salinity on Ch₄/C₂H₆ Hydrate Particle-Surface Interactions. *Phys Chem Chem Phys* **2017**, *19*, 13307-13315.
46. Hu, S. J.; Koh, C. A. Interfacial Properties and Mechanisms Dominating Gas Hydrate Cohesion and Adhesion in Liquid and Vapor Hydrocarbon Phases. *Langmuir* **2017**, *33*, 11299-11309.
47. Hu, S. J.; Koh, C. A. Ch₄/C₂H₆ Gas Hydrate Interparticle Interactions in the Presence of Anti-Agglomerants and Salinity. *Fuel* **2020**, *269*, 117208.
48. Hu, S.; Vo, L.; Monteiro, D.; Bodnar, S.; Prince, P.; Koh, C. A. Structural Effects of Gas Hydrate Antiagglomerant Molecules Oninterfacial Interparticle Force Interactions. *Langmuir* **2021**, *37*, 1651-1661.
49. Bui, T.; Monteiro, D.; Vo, L.; Striolo, A. Synergistic and Antagonistic Effects of Aromatics on the Agglomeration of Gas Hydrates. *Sci Rep-Uk* **2020**, *10*, 1-11.
50. Sicard, F.; Bui, T.; Monteiro, D.; Lan, Q.; Ceglie, M.; Burrell, C.; Striolo, A. Emergent Properties of Antiagglomerant Films Control Methane Transport: Implications for Hydrate Management. *Langmuir* **2018**, *34*, 9701-9710.
51. Takeuchi, F.; Hiratsuka, M.; Ohmura, R.; Alavi, S.; Sum, A. K.; Yasuoka, K. Water Proton Configurations in Structures I, II, and H Clathrate Hydrate Unit Cells. *J Chem Phys* **2013**, *138*, 124504
52. Abascal, J. L. F.; Sanz, E.; Fernandez, R. G.; Vega, C. A Potential Model for the Study of Ices and Amorphous Water: Tip4p/Ice. *J Chem Phys* **2005**, *122*, 234511.
53. Walsh, M. R.; Koh, C. A.; Sloan, E. D.; Sum, A. K.; Wu, D. T. Microsecond Simulations of Spontaneous Methane Hydrate Nucleation and Growth. *Science* **2009**, *326*, 1095-1098.
54. Wang, J. M.; Wolf, R. M.; Caldwell, J. W.; Kollman, P. A.; Case, D. A. Development and Testing of a General Amber Force Field. *J Comput Chem* **2004**, *25*, 1157-1174.
55. Case, D. A.; Babin, V.; Berryman, J. T.; Betz, R. M.; Cai, Q.; Cerutti, D. S.; Cheatham, T. E. I.; Darden, T. A.; Duke, R. E.; Gohlke, H.; Goetz, A. W.; Gusarov, S.; Homeyer, N.; Janowski, P.; Kaus, J.; Kolossváry, I.; Kovalenko, A.; Lee, T. S.; LeGrand, S.; Luchko, T. L., R.; Madej, B.; Merz, K. M.; Paesani, F.; Roe, D. R.; Roitberg, A.; Sagui, C.; Salomon-Ferrer, R.; Seabra, G.; Simmerling, C. L.; Smith, W.; Swails, J.; Walker, R. C.; Wang, J.; Wolf, R. M.; Wu, X.; Kollman, P. A., *Amber 14*: University of California, San Francisco, 2014.
56. Martin, M. G.; Siepmann, J. I. Transferable Potentials for Phase Equilibria. 1. United-Atom Description of N-Alkanes. *J Phys Chem B* **1998**, *102*, 2569-2577.
57. Smith, D. E.; Dang, L. X. Computer-Simulations of NaCl Association in Polarizable Water. *J Chem Phys* **1994**, *100*, 3757-3766.
58. Mamatkulov, S.; Fyta, M.; Netz, R. R. Force Fields for Divalent Cations Based on Single-Ion and Ion-Pair Properties. *J Chem Phys* **2013**, *138*.
59. Hartkamp, R.; Coasne, B. Structure and Transport of Aqueous Electrolytes: From Simple Halides to Radionuclide Ions. *J Chem Phys* **2014**, *141*.
60. Eastwood, J. W.; Hockney, R. W.; Lawrence, D. N. P3m3dp - the 3-Dimensional Periodic Particle-Particle-Particle-Mesh Program. *Comput Phys Commun* **1980**, *19*, 215-261.
61. Allen, M. P.; Tildesley, D. J., *Computer Simulation of Liquids*; Oxford University Press: Oxford, UK, 2004.

62. Abraham, M. J.; Murtola, T.; Schulz, R.; Páll, S.; Smith, J. C.; Hess, B.; Lindahl, E. Gromacs: High Performance Molecular Simulations through Multi-Level Parallelism from Laptops to Supercomputers. *SoftwareX* **2015**, *1*, 19-25.
63. Hub, J. S.; de Groot, B. L.; van der Spoel, D. G_Wham-a Free Weighted Histogram Analysis Implementation Including Robust Error and Autocorrelation Estimates. *J Chem Theory Comput* **2010**, *6*, 3713-3720.
64. Griffiths, M. Z.; Shinoda, W. Analyzing the Role of Surfactants in the Colloidal Stability of Nanoparticles in Oil through Coarse-Grained Molecular Dynamics Simulations. *J Phys Chem B* **2021**.
65. Vo, M. D.; Papavassiliou, D. V. Interaction between Polymer-Coated Carbon Nanotubes with Coarse-Grained Computations. *Chem Phys Lett* **2017**, *685*, 77-83.
66. Motulsky, H. J.; Brown, R. E. Detecting Outliers When Fitting Data with Nonlinear Regression - a New Method Based on Robust Nonlinear Regression and the False Discovery Rate. *Bmc Bioinformatics* **2006**, *7*, 123.
67. McCulfor, J.; Himes, P.; Anklam, M. R. The Effects of Capillary Forces on the Flow Properties of Glass Particle Suspensions in Mineral Oil. *Aiche J* **2011**, *57*, 2334-2340.
68. Anklam, M. R.; York, J. D.; Helmerich, L.; Firoozabadi, A. Effects of Antiagglomerants on the Interactions between Hydrate Particles. *Aiche J* **2008**, *54*, 565-574.
69. Rabinovich, Y. I.; Esayanur, M. S.; Moudgil, B. M. Capillary Forces between Two Spheres with a Fixed Volume Liquid Bridge: Theory and Experiment. *Langmuir* **2005**, *21*, 10992-10997.
70. Kaimaki, D. M.; Smith, B. E.; Durkan, C. On the Use of Nanomechanical Atomic Force Microscopy to Characterise Oil-Exposed Surfaces. *Rsc Adv* **2018**, *8*, 6680-6689.
71. Sicard, F.; Striolo, A. Role of Structural Rigidity and Collective Behaviour in the Molecular Design of Gas Hydrates Anti-Agglomerants. *arXiv:2012.09765* **2021**.
72. Nayar, D.; Yadav, H. O. S.; Jabes, B. S.; Chakravarty, C. Relating Structure, Entropy, and Energy of Solvation of Nanoscale Solutes: Application to Gold Nanoparticle Dispersions. *J Phys Chem B* **2012**, *116*, 13124-13132.
73. Srivastava, A.; Debnath, A. Asymmetry and Rippling in Mixed Surfactant Bilayers from All-Atom and Coarse-Grained Simulations: Interdigitation and Per Chain Entropy. *The Journal of Physical Chemistry B* **2020**, *124*, 6420-6436.
74. Schlitter, J. Estimation of Absolute and Relative Entropies of Macromolecules Using the Covariance-Matrix. *Chem Phys Lett* **1993**, *215*, 617-621.
75. Schafer, H.; Mark, A. E.; van Gunsteren, W. F. Absolute Entropies from Molecular Dynamics Simulation Trajectories. *J Chem Phys* **2000**, *113*, 7809-7817.
76. Andricioaei, I.; Karplus, M. On the Calculation of Entropy from Covariance Matrices of the Atomic Fluctuations. *J Chem Phys* **2001**, *115*, 6289-6292.
77. Wilson, N. T.; Johnston, R. L. Modelling Gold Clusters with an Empirical Many-Body Potential. *Eur Phys J D* **2000**, *12*, 161-169.
78. Hikiri, S.; Yoshidome, T.; Ikeguchi, M. Computational Methods for Configurational Entropy Using Internal and Cartesian Coordinates. *J Chem Theory Comput* **2016**, *12*, 5990-6000.
79. Baron, R.; de Vries, A. H.; Hunenberger, P. H.; van Gunsteren, W. F. Comparison of Atomic-Level and Coarse-Grained Models for Liquid Hydrocarbons from Molecular Dynamics Configurational Entropy Estimates. *J Phys Chem B* **2006**, *110*, 8464-8473.
80. Orozco, M.; Luque, F. J. Theoretical Methods for the Description of the Solvent Effect in Biomolecular Systems. *Chem Rev* **2000**, *100*, 4187-4225.
81. Lynden-Bell, R. M.; Giovambattista, N.; Debenedetti, P. G.; Head-Gordon, T.; Rossky, P. J. Hydrogen Bond Strength and Network Structure Effects on Hydration of Non-Polar Molecules. *Phys Chem Chem Phys* **2011**, *13*, 2748-2757.

82. Arnold, T.; Thomas, R. K.; Castro, M. A.; Clarke, S. M.; Messe, L.; Inaba, A. The Crystalline Structures of the Even Alkanes Hexane, Octane, Decane, Dodecane and Tetradecane Monolayers Adsorbed on Graphite at Submonolayer Coverages and from the Liquid. *Phys Chem Chem Phys* **2002**, *4*, 345-351.
83. Naullage, P. M.; Bertolazzo, A. A.; Molinero, V. How Do Surfactants Control the Agglomeration of Clathrate Hydrates? *Acs Central Sci* **2019**, *5*, 428-439.
84. Nagai, T.; Tsurumaki, S.; Urano, R.; Fujimoto, K.; Shinoda, W.; Okazaki, S. Position-Dependent Diffusion Constant of Molecules in Heterogeneous Systems as Evaluated by the Local Mean Squared Displacement. *J Chem Theory Comput* **2020**, *16*, 7239-7254.
85. Berne, B. J.; Borkovec, M.; Straub, J. E. Classical and Modern Methods in Reaction-Rate Theory. *J Phys Chem-Us* **1988**, *92*, 3711-3725.
86. Hummer, G. Position-Dependent Diffusion Coefficients and Free Energies from Bayesian Analysis of Equilibrium and Replica Molecular Dynamics Simulations. *New J Phys* **2005**, *7*, 34.
87. Gaalswyk, K.; Awoonor-Williams, E.; Rowley, C. N. Generalized Langevin Methods for Calculating Transmembrane Diffusivity. *J Chem Theory Comput* **2016**, *12*, 5609-5619.

Correlating Antiagglomerant Performance with Gas Hydrate Cohesion

Anh Phan,¹ Michail Stamatakis,¹ Carolyn A. Koh² and Alberto Striolo^{1,*}

¹Department of Chemical Engineering, University College London, London WC1E 7JE, UK

²Center for Hydrate Research, Chemical & Biological Engineering Department, Colorado School of Mines, Golden, Colorado 80401, United States

Supplementary Information

*Corresponding Author

a.striolo@ucl.ac.uk

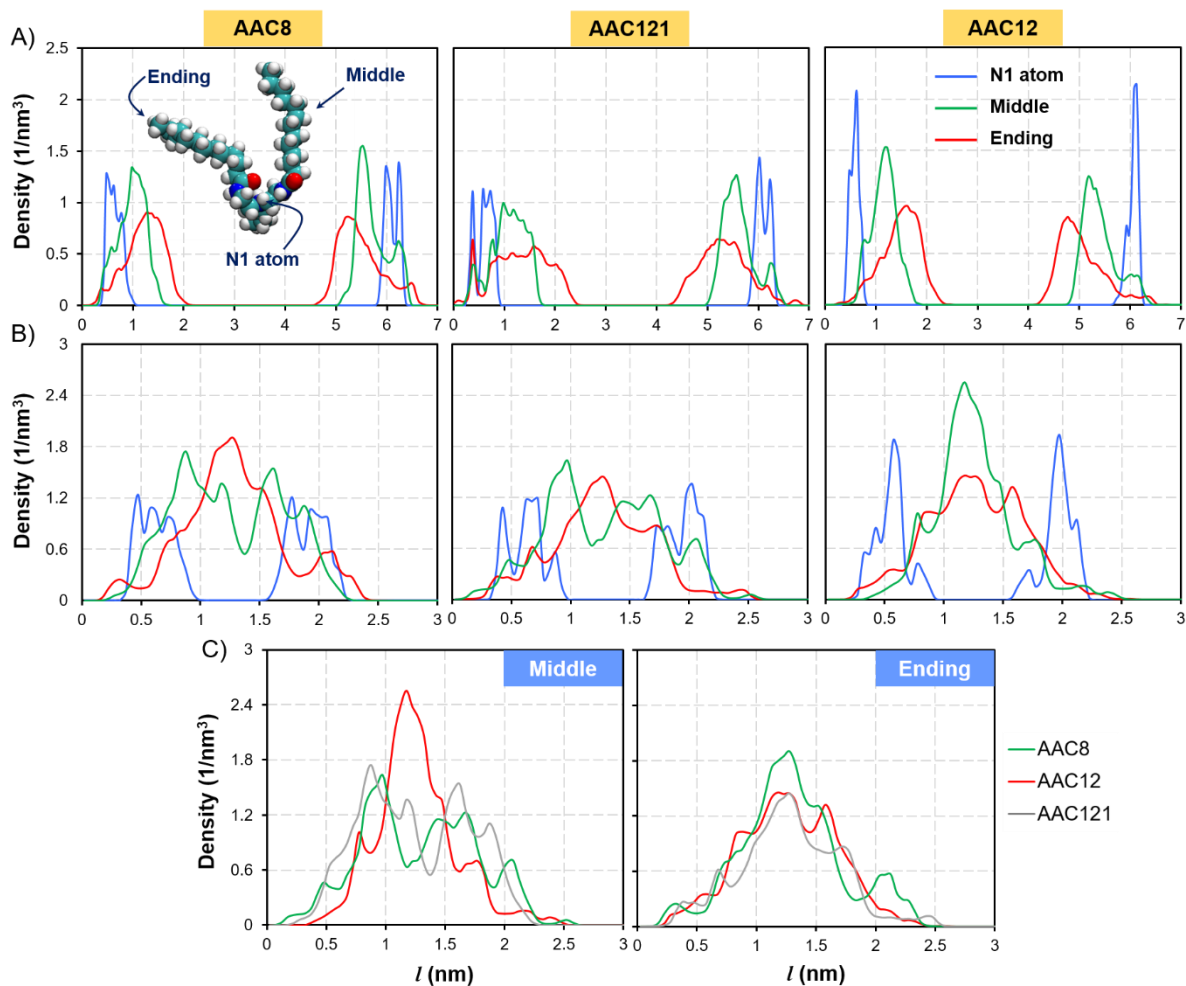


Figure S1. Density profiles of AA layers confined between two hydrate particles when they are further away from each other (panel A) and when they are brought at distance $l = 2.51$ nm (panel B), where the repulsive barrier is located in the PMF profile obtained for systems with AAC12, as shown in **Figure 2** of the main text. Results are shown for N^+ atom (blue), middle (green) and ending (red) carbon atoms of AAC8 (left), AAC121 (middle), and AAC12 (right) tails along the Z-direction (perpendicular to the hydrate surfaces). C) Density profiles of middle (left) and ending (right) carbon atoms of AAC8 (green), AAC121 (grey), and AAC12 (red) tails along the Z-direction when the two hydrate particles are brought close near one another at distance $l = 2.51$ nm

In **Figure S1**, we report the results of density profiles of AA layers confined between the two hydrate particles when they are far from each other (panel A) and when they are at distance $l = 2.51$ nm (panel B). Results are shown for N^+ atom (see **Figure 1B** in the main text) (blue), middle (green) and end (red) carbon atoms of AAC8 (left), AAC121 (middle), and AAC12 (right) tails along the Z-direction (perpendicular to the hydrate surfaces). We do not observe significant differences in the density profiles for different AAs, *e.g.*, AAC8, AAC121, and AAC12 when the two hydrate particles are far from each other (panel A). However, when the two hydrate particles are at $l = 2.51$ nm, the density peak obtained for the system with AAC12 is noticeably more pronounced and narrower compared to those found for

systems with AAC8 and AAC121 (left, panel C). Note that the total number of middle carbon atoms of tails of AAC8, AAC121 and AAC12 are the same. This suggests that AAC12 might not be as flexible as the other AAs considered, i.e., AAC8 and AAC121; the presence of pronounced density peak for the middle carbon atoms of AAC12 tails when the two hydrate particles are near each other could be related to the free energy barrier in the PMF results. We do not observe significant differences in the results for density profiles obtained for the ending carbon atoms of tails of AAC8 (green), AAC121 (grey) and AAC12 (red) when the two hydrate particles are brought near one another.

In **Table S1**, we report data extracted from the PMF profiles, shown in **Figure 2** of the main text.

Table S1. Locations of minimum and local maxima in the PMF profiles and locations where attraction initiates.

	Minimum (Å)		Local Maximum (Å)		Coalescence Initiation (Å)	
	C12	C7	C12	C7	C12	C7
AAC8-0.44	12.5	13.6			26.9	26.9
AAC12-0.44	13.5	11.1	21.6	23.7	17.2	20.6
AAC121-0.44	13.3	11.5	25.5	26.5	24.4	24.9
AAC171-0.28	10.5	11.5	23.5	25.4	20.0	24.5
AAC171-0.44	10.8	13.6	20.2	21.6	14.4	17.4

The force–distance profiles shown in **Figure 3** of the main text are reminiscent of a Lennard-Jones force (with parameters ε and σ) superimposed to a repulsive peak (parameters r_o , b , and n), yielding the following expression:¹

$$F = 4\varepsilon \left(\frac{12\sigma^{12}}{r^{13}} - \frac{6\sigma^6}{r^7} \right) \times \left(1 - \sqrt{\pi} \exp \left[\frac{-(r-r_o)^2}{b} \right] \times n \right) \quad (1)$$

The procedure of fitting simulated force data points while removing outliers follows three steps:

1. Fit simulated force data points to Eq. (1) via adjusting the parameters ε , σ , r_o , b , and n employing a non-linear regression with the Levenberg-Marquardt algorithm.
2. Examine the residuals of the fit and identify whether one or more values are outliers. To do this, we applied the method of outlier identification developed by Motulsky and Brown² based on the False

Discovery Rate (FDR) approach of testing for multiple comparisons. The details about the numerical procedure to detect outliers follows these steps are described by Motulsky and Brown.²

3. Remove the outliers and implement non-linear regression on the remaining data.
4. Employ the chi-squared test and degrees of freedom for fitting parameters to perform a ‘goodness of fit’ test. An iterative procedure that minimizes the reduced chi-square value to obtain the optimal parameter values is implemented during the nonlinear curve fitting performance. The reduced chi-square was calculated by dividing the residual sum of squares by the degrees of freedom.
5. Complete the fitting with a minimal value of reduced chi-square and a high value of the coefficient of determination (R^2) for the model parameters.

In **Table S2**, we report the resultant fitted parameters.

Table S2. Values of the fitting parameters of the force – distance curve model described in Eq. (1) for all systems considered

	ϵ (kcal.mol ⁻¹ .nm ⁻¹)	σ (nm)	r_o (nm)	b (nm ²)	n
AAC8 – C12	0.115 ± 0.005	1.108 ± 0.009	1.950 ± 0.016	0.190 ± 0.002	-1.45E6 ± 0.07E6
AAC12 – C12	0.008 ± 0.002	1.934 ± 0.024	2.500 ± 0.031	0.150 ± 0.002	-1.15E3 ± 0.31E3
AAC121 – C12	0.015 ± 0.002	1.190 ± 0.003	1.950 ± 0.005	0.190 ± 0.001	-1.84E6 ± 0.27E6
AAC171 – C12	1.137 ± 0.096	0.854 ± 0.002	1.950 ± 0.005	0.230 ± 0.001	-1.09E1 ± 0.09E1
AAC8 – C7	0.324 ± 0.064	1.212 ± 0.005	1.950 ± 0.008	0.190 ± 0.001	-1.10E2 ± 0.22E2
AAC12 – C7	0.466 ± 0.100	1.005 ± 0.008	1.950 ± 0.016	0.190 ± 0.002	-2.07E2 ± 0.45E2
AAC121 – C7	0.098 ± 0.011	1.032 ± 0.006	1.950 ± 0.011	0.190 ± 0.001	-1.28E3 ± 0.14E3
AAC171 – C7	0.046 ± 0.003	1.133 ± 0.004	1.950 ± 0.007	0.190 ± 0.001	-1.39E3 ± 0.10E3

References

1. Vo, M. D.; Papavassiliou, D. V. Interaction between Polymer-Coated Carbon Nanotubes with Coarse-Grained Computations. *Chem Phys Lett* **2017**, *685*, 77-83.
2. Motulsky, H. J.; Brown, R. E. Detecting Outliers When Fitting Data with Nonlinear Regression - a New Method Based on Robust Nonlinear Regression and the False Discovery Rate. *Bmc Bioinformatics* **2006**, *7*.